The Arnold–Winther mixed FEM in linear elasticity. Part I: Implementation and numerical verification ☆

C. Carstensen [a,*], D. Günther [a], J. Reininghaus [a], J. Thiele [b]

[a] *Department of Mathematics, Humboldt-Universität zu Berlin, Unter den Linden 6, D-10099 Berlin, Germany*
[b] *BMW Group, Hufelandstraße 8a, 80788 München, Germany*

Abstract

Following some de Rham complex, Arnold and Winther have recently proposed a symmetric mixed finite element method (MFEM) in linear elasticity. This paper describes the implementation of the symmetric MFEM and its 30×30 local stress stiffness matrices and studies the implementation of the lowest-order scheme for general boundary conditions. Numerical experiments in model examples in computational mechanics illustrate the robust locking-free convergence behavior and support the theoretically predicted experimental convergence rates.
© 2008 Elsevier B.V. All rights reserved.

1. Introduction

The paper investigates the mixed finite element solutions of the 2D Lamé system in linear elasticity due to Arnold and Winther [3] for some plane elastic body $\Omega \subset \mathbb{R}^2$ with boundary $\partial\Omega = \Gamma = \Gamma_D \cup \Gamma_N$ decomposed into some closed part Γ_D of positive length for displacement boundary conditions u_D and its complement $\Gamma_N = \Gamma \setminus \Gamma_D$ subject to applied surface loads g with exterior unit normal v. Given a volume force $f : \Omega \to \mathbb{R}^2$ and a traction $g : \Gamma_N \to \mathbb{R}^2$, we seek the displacement field $u \in H^1(\Omega; \mathbb{R}^2)$ and the stress tensor $\sigma \in H(\mathrm{div}, \Omega; \mathbb{S})^2$ satisfying

$$
\begin{aligned}
-\,\mathrm{div}\,\sigma = f \quad &\text{and} \quad \sigma = \mathbb{C}\varepsilon(u) \quad \text{in } \Omega, \\
u = u_D \quad &\text{on } \Gamma_D \quad \text{and} \quad \sigma v = g \quad \text{on } \Gamma_N.
\end{aligned}
\tag{1.1}
$$

Here and throughout, $\varepsilon(v) = \frac{1}{2}\left(\nabla v + (\nabla v)^{\mathrm{T}}\right)$ denotes the linearized Green strain tensor, $\mathbb{C}$ is the symmetric fourth

order bounded and positive definite elasticity tensor, and $\mathbb{S} := \mathbb{R}^{2\times2}_{\mathrm{sym}}$ denotes the space of symmetric matrices. As a consequence of Korn's inequality and the Lax–Milgram lemma, problem (1.1) has a unique solution $(\sigma, u) \in L^2(\Omega; \mathbb{S}) \times H^1(\Omega; \mathbb{R}^2)$.

For nearly incompressible materials, i.e., for a Poisson ratio near to 1/2, the Lamé constant λ in $\mathbb{C}$ is very large and the standard computation of a displacement finite element solution u_h fails in the sense of locking: The constant $C(\lambda)$ in the error estimate

$$
\|\mathbb{C}^{1/2}\varepsilon(u - u_h)\|_{L^2(\Omega)} \leqslant C(\lambda)h^{\alpha}
\tag{1.2}
$$

(for small mesh-sizes h) tends to infinity as $\lambda \to \infty$; we refer to [10] for a numerical illustration. The design of mixed finite element methods overcomes this locking in the sense that, in different norms in the a priori estimates, the constant $C(\lambda)$ in (1.2) remains bounded as $\lambda \to \infty$.

The design of mixed FEM (MFEM) in elasticity faces some difficulties with the symmetry constraint explained in [6] which led to the former discretisations with unsymmetric stresses [1,9,10,12]. This paper is devoted to a recent suggestion of a symmetric MFEM due to Arnold and

Winther [3] illustrated in Fig. 1.1 and its algorithmic realisation.

For completeness we restate the central convergence results of [3] for the lowest-order case implemented in this paper with

$$\sigma \in H(\mathrm{div}, \Omega, \mathbb{S}) := L^2(\Omega; \mathbb{S}) \cap H(\mathrm{div}, \Omega)^2 \quad \text{and}$$

$$u \in L^2(\Omega; \mathbb{R}^2),$$

with their discrete counterparts $\sigma_h \in \Sigma_h$, defined in Section 2, and the (discontinuous) piecewise affine displacement $u_h \in \mathscr{P}_1(\mathscr{T}; \mathbb{R}^2)$.

Theorem 1 (Arnold and Winther [3]). *There exists some constant c which is independent of λ and independent of the sufficiently small mesh-size h such that, for sufficiently smooth σ and u, there holds*

$$\|\sigma - \sigma_h\|_{L^2(\Omega)} \leqslant ch^m \|\sigma\|_{H^m(\Omega)} \quad \text{for } 1 \leqslant m \leqslant 3,$$

$$\|\mathrm{div}(\sigma - \sigma_h)\|_{L^2(\Omega)} \leqslant ch^m \|\mathrm{div}\,\sigma\|_{H^m(\Omega)} \quad \text{for } 0 \leqslant m \leqslant 2,$$

$$\|u - u_h\|_{L^2(\Omega)} \leqslant ch^m \|u\|_{H^{m+1}(\Omega)} \quad \text{for } 1 \leqslant m \leqslant 2.$$

The remaining parts of the paper are organized as follows. Section 2 describes some notation, the discrete subspaces, the weak form, and the implementation of the subspaces Σ_h and V_h and the MFEM. Sections 3 and 4 contain some numerical examples to study experimental convergence rates for uniform and graded meshes and provides numerical evidence of the locking-free convergence behavior of Theorem 1. Some remarks in Section 5 conclude this paper.

2. Mixed finite element formulation

2.1. Weak mixed formulation

This paper exploits standard notation for Lebesgue $L^2(\Omega)$ and Sobolev spaces $H^1(\Omega)$ and concerns the spaces
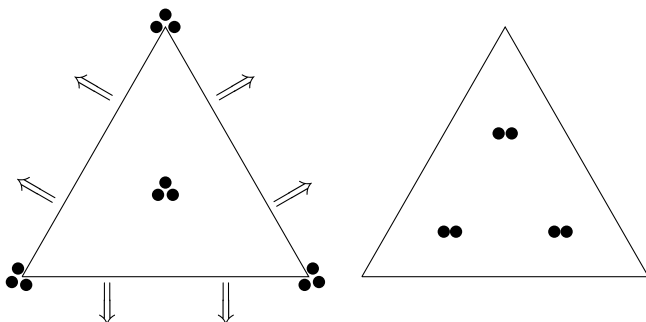

Fig. 1.1. Illustration of the 30 degrees of freedom of the Arnold–Winther MFEM for the lowest-order stresses (left) and displacements (right). The three dots at the three vertices of the triangle (left) represent point evaluations for all three components of $\sigma \in \mathbb{S}$ while the three dots in the interior denote the integral means for all three components. The arrows represent the moments of order $\leqslant 1$ of the two components of the boundary stress vector σv. The six dots in the triangle (right) represent the degrees of freedom for the two components of the (globally discontinuous) P_1 displacement approximation.

$$\Sigma := H(\mathrm{div}, \Omega)^2, \quad \mathscr{V} := L^2(\Omega; \mathbb{R}^2), \quad \mathbb{S} := \mathbb{R}^{2 \times 2}_{sym},$$

$$\Sigma_g := \{\tau \in H(\mathrm{div}, \Omega)^2 \cap L^2(\Omega; \mathbb{S}) \,|\,$$

$$\int_{\Gamma_N} \psi \cdot (\tau v) \mathrm{d}s_x = \int_{\Gamma_N} \psi \cdot g \mathrm{d}s_x \quad \text{for all } \psi \in \Sigma\},$$

$$H(\mathrm{div}, \Omega) := \{q \in L^2(\Omega; \mathbb{R}^2) \,|\, \mathrm{div}\, q \in L^2(\Omega)\}.$$

The weak formulation of (1.1) reads: Given the data $u_D \in H^1(\Omega; \mathbb{R}^2)$, $f \in L^2(\Omega; \mathbb{R}^2)$, $g \in L^2(\Gamma_N; \mathbb{R}^2)$, seek $(\sigma, u) \in \Sigma_g \times \mathscr{V}$ with

$$\int_\Omega \sigma : \mathbb{C}^{-1} \tau \mathrm{d}x + \int_\Omega u \cdot \mathrm{div}\,\tau \mathrm{d}x$$

$$= \int_{\Gamma_D} u_D \cdot (\tau v) \mathrm{d}s_x \quad \text{for all } \tau \in \Sigma, \qquad (2.1)$$

$$\int_\Omega v \cdot \mathrm{div}\,\sigma \mathrm{d}x = - \int_\Omega f \cdot v \mathrm{d}x \quad \text{for all } v \in \mathscr{V}.$$

Here and throughout, $\cdot$ and : denote the scalar product in $\mathbb{R}^2$ and $\mathbb{S} := \mathbb{R}^{2 \times 2}_{sym}$.

2.2. Arnold–Winther MFEM

On each triangle T in the regular triangulation $\mathscr{T}$, the local discrete counterparts of Σ and $\mathscr{V}$ read

$$\Sigma_T = \{\tau \in \mathscr{P}_3(T; \mathbb{S}) \,|\, \mathrm{div}\,\tau \in \mathscr{P}_1(T; \mathbb{R}^2)\} \quad \text{and}$$

$$V_T = \mathscr{P}_1(T; \mathbb{R}^2). \qquad (2.2)$$

For each triangle $T = \mathrm{conv}(P_1, P_2, P_3)$ with vertices P_1, P_2, and $P_3 \in \mathbb{R}^2$ with the barycentric coordinates λ_1, λ_2, and λ_3 on T

$$\lambda_j(P_k) = \delta_{jk} \quad \text{for}, k = 1, 2, 3 \qquad (2.3)$$

(with Kronecker's delta δ_{jk}) form the nodal basis of $\mathscr{P}_1(T; \mathbb{R})$. One basis $\phi_1, \dots, \phi_{10}$ of $\mathscr{P}_3(T, \mathbb{R})$ reads

$$\phi_1 = \lambda_1, \quad \phi_2 = \lambda_2, \quad \phi_3 = \lambda_3, \quad \phi_4 = \lambda_1 \lambda_2,$$

$$\phi_5 = \lambda_2 \lambda_3, \quad \phi_6 = \lambda_3 \lambda_1, \quad \phi_7 = \lambda_1 \lambda_2 (\lambda_1 - \lambda_2),$$

$$\phi_8 = \lambda_2 \lambda_3 (\lambda_2 - \lambda_3), \quad \phi_9 = \lambda_1 \lambda_3 (\lambda_3 - \lambda_1), \quad \phi_{10} = \lambda_1 \lambda_2 \lambda_3.$$

An arbitrary function $\sigma \in \mathscr{P}_3(T, \mathbb{S})$ assumes the form

$$\sigma := \sum_{k=1}^{10} \phi_k \begin{pmatrix} a_k & c_k \\ c_k & b_k \end{pmatrix} \qquad (2.4)$$

with 30 coefficients $a_1, \dots, a_{10}$, $b_1, \dots, b_{10}$, and $c_1, \dots, c_{10}$. Since Σ_T has dimension 24, one needs to design 24 basis functions of Σ_T in terms of the real coefficients a_k, b_k, c_k. According to [3], the natural degrees of freedom $\xi_1, \dots, \xi_{24}$ on the triangle among the coefficients in (2.4) are specified in (i)–(iii) as follows:

  (i) the values of the three components of σ at each vertex P_j of T (9 degrees of freedom), i.e.,

$$\sigma(P_j) = \begin{pmatrix} \xi_{3j-2} & \xi_{3j} \\ \xi_{3j} & \xi_{3j-1} \end{pmatrix};$$

(ii) the values of the moments of degree 0 and 1 of the two normal components of σ on each edge E_j of T (12 degrees of freedom), i.e.,

$$|E_j|^{-1} \int_{E_j} \sigma v_{E_j} \mathrm{d}s_x = \begin{pmatrix} \xi_{4j+6} \\ \xi_{4j+7} \end{pmatrix},$$

$$|E_j|^{-2} \int_{E_j} ((x - \mathrm{mid}(E_j))\tau_{E_j})\sigma v_{E_j} \mathrm{d}s_x = \begin{pmatrix} \xi_{4j+8} \\ \xi_{4j+9} \end{pmatrix}.$$

Here and throughout this paper, $\tau_{E_j} \perp v_{E_j}$ denotes the unit tangential vector along the edge E_j with mid-point $\mathrm{mid}(E_j)$;

(iii) the value of the three components of the integral mean of σ on T (3 degrees of freedom), i.e.,

$$|T|^{-1} \int_T \sigma \mathrm{d}x = \begin{pmatrix} \xi_{22} & \xi_{24} \\ \xi_{24} & \xi_{23} \end{pmatrix}.$$

The degrees of freedom $\xi_{25},\ldots,\xi_{30}$ represent the sum of coefficients of the P_3 basis which belong to the quadratic terms of $\mathrm{div}\,\sigma$. The restriction $\mathrm{div}\,\sigma \in \mathscr{P}_1(T;\mathbb{R}^2)$ implies that these degrees of freedom must be zero.

The complete mapping $(a_1, b_1, c_1,\ldots, a_{10}, b_{10}, c_{10}) \mapsto (\xi_1, \xi_2,\ldots,\xi_{30})$ is given through the 30×30 matrix C specified below. Then the coefficients of the basis functions σ_j are given by solving the linear system of equations

$$C(a_1, b_1, c_1,\ldots, a_{10}, b_{10}, c_{10})^{\mathrm{T}} = (\xi_1, \xi_2,\ldots,\xi_{30})^{\mathrm{T}}. \qquad (2.5)$$

A direct calculation eventually leads to the following representation of the 30×30 matrix C given in the sequel. Here and throughout the paper, 0 represents a zero block. Since all blocks are rectangular, the dimensions of this block 0 follows from consistency, e.g., the three symbols 0 in the first row of C have the respective dimensions 9×9, 9×9, and 9×3. The matrix C is partitioned as

$$C = \frac{1}{60} \begin{pmatrix} 60 I_9 & 0 & 0 & 0 \\ R_{30,5} & S_{10,0} & S_{0,-1} & 0 \\ 20\widetilde{I} & 5\widetilde{I} & 0 & I_3 \\ 0 & 0 & \widetilde{Q} & Q_4 \end{pmatrix} \qquad (2.6)$$

with the $k \times k$ identity matrix I_k, $\widetilde{I} = (I_3,\ I_3,\ I_3)$, $\widetilde{Q} = (Q_1,\ Q_2,\ Q_3)$, and

$$Q_\ell = 60\mathrm{diam}(T) \begin{pmatrix} D_x W^{(\ell)} & 0 & D_y W^{(\ell)} \\ 0 & D_y W^{(\ell)} & D_x W^{(\ell)} \end{pmatrix}$$

for

$$W^{(1,\ldots,4)} = \begin{pmatrix} 3(\lambda_1 - \lambda_2) & -\lambda_3 & \lambda_3 & \lambda_3 \\ \lambda_1 & 3(\lambda_2 - \lambda_3) & -\lambda_1 & \lambda_1 \\ -\lambda_2 & \lambda_2 & 3(\lambda_3 - \lambda_1) & \lambda_2 \end{pmatrix}.$$

The matrices $R_{k,m}$ and $S_{k,m}$ are defined by

$$R_{k,m} = \begin{pmatrix} kN^{(1)} & kN^{(1)} & 0 \\ -mN^{(1)} & mN^{(1)} & 0 \\ 0 & kN^{(2)} & kN^{(2)} \\ 0 & -mN^{(2)} & mN^{(2)} \\ kN^{(3)} & 0 & kN^{(3)} \\ mN^{(3)} & 0 & -mN^{(3)} \end{pmatrix},$$

$$S_{k,m} = \begin{pmatrix} kN^{(1)} & 0 & 0 \\ mN^{(1)} & 0 & 0 \\ 0 & kN^{(2)} & 0 \\ 0 & mN^{(2)} & 0 \\ 0 & 0 & kN^{(3)} \\ 0 & 0 & mN^{(3)} \end{pmatrix}$$

with $N^{(j)} = \begin{pmatrix} v_1^{(j)} & 0 & v_2^{(j)} \\ 0 & v_2^{(j)} & v_1^{(j)} \end{pmatrix}$ for the kth component $v_k^{(j)}$ of the outer unit normal $v^{(j)}$ on the jth edge E_j of the triangle of Fig. 2.1. Note that the matrix C is mesh-size independent because of the appropriate scaling of the degrees of freedom.

Finally, the piecewise affine and globally discontinuous ansatz functions for $\mathscr{V}_{\mathscr{T}} = P_1(\mathscr{T};\mathbb{R}^2)$ read $(\lambda_1, 0), (\lambda_2, 0), (\lambda_3, 0), (0, \lambda_1), (0, \lambda_2), (0, \lambda_3)$ in terms of the barycentric coordinates λ_1, λ_2, and λ_3 of $T \in \mathscr{T}$.

2.3. Local stiffness matrix

For each triangle T, its local stiffness matrix

$$A_T := \begin{pmatrix} A^{(1)} & A^{(2)} \\ A^{(2)T} & 0 \end{pmatrix} \in \mathbb{R}_{\mathrm{sym}}^{30 \times 30} \qquad (2.7)$$
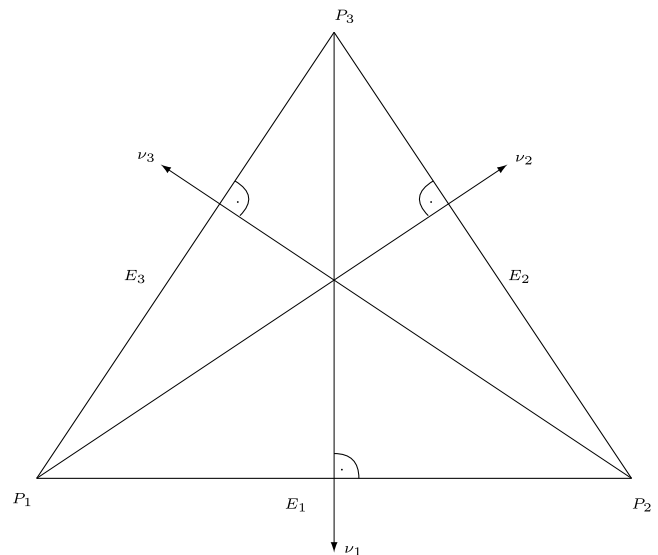

Fig. 2.1. Triangle $T = \mathrm{conv}\{P_1, P_2, P_3\}$ with vertices P_1, P_2, P_3 (ordered counterclockwise by convention) and edges $E_1 = \mathrm{conv}\{P_1,\ P_2\}$, $E_2 = \mathrm{conv}\{P_2, P_3\}$, $E_3 = \mathrm{conv}\{P_3, P_1\}$ of respective lengths $|E_1|, |E_2|, |E_3|$.

is defined by

$$A_{jk}^{(1)} := \int_T \mathbb{C}^{-1}\sigma_j : \sigma_k \mathrm{d}x \quad \text{for } j,k = 1,\dots 24; \tag{2.8}$$

$$A_{jk}^{(2)} := \int_T \operatorname{div}\sigma_j \cdot v_k \mathrm{d}x \quad \text{for } j = 1,\dots 24, k = 1,\dots,6. \tag{2.9}$$

Following the definition in [7], the fourth-order material tensor $\mathbb{C}$ and its inverse read

$$\mathbb{C} := \begin{pmatrix} 2\mu+\lambda & \lambda & 0 \\ \lambda & 2\mu+\lambda & 0 \\ 0 & 0 & \mu \end{pmatrix} \quad \text{and}$$

$$\mathbb{C}^{-1} = \begin{pmatrix} \frac{\lambda+2\mu}{4\mu(\lambda+\mu)} & \frac{-\lambda}{4\mu(\lambda+\mu)} & 0 \\ \frac{-\lambda}{4\mu(\lambda+\mu)} & \frac{\lambda+2\mu}{4\mu(\lambda+\mu)} & 0 \\ 0 & 0 & 1/\mu \end{pmatrix}.$$

Let σ_j and σ_k, $j,k = 1,\dots,24$, denote two basis functions constructed above. In Voigt notation, they are both of the format

$$\sigma_j = \begin{pmatrix} \alpha_j & \gamma_j \\ \gamma_j & \beta_j \end{pmatrix} \quad \text{and} \quad \begin{pmatrix} \alpha_j \\ \beta_j \\ \gamma_j \end{pmatrix} := \begin{pmatrix} \sum_{\ell=1}^{10} a_\ell^{(j)}\phi_\ell \\ \sum_{\ell=1}^{10} b_\ell^{(j)}\phi_\ell \\ \sum_{\ell=1}^{10} c_\ell^{(j)}\phi_\ell \end{pmatrix} \tag{2.10}$$

for the coefficients from (2.5). The entry $A_{jk}^{(1)}$ is then computed by

$$\begin{aligned} A_{jk}^{(1)} &= \int_T \mathbb{C}^{-1}\sigma_j : \sigma_k \mathrm{d}x = (\alpha_j, \beta_j, \gamma_j)\mathbb{C}^{-1}(\alpha_k, \beta_k, \gamma_k)^T \\ &= \mathbb{C}_{1,1}^{-1}\int_T(\alpha_j\alpha_k + \beta_j\beta_k)\mathrm{d}x + \mathbb{C}_{1,2}^{-1}\int_T(\alpha_j\beta_k + \beta_j\alpha_k)\mathrm{d}x \\ &\quad + \mathbb{C}_{3,3}^{-1}\int_T \gamma_j\gamma_k \mathrm{d}x. \end{aligned}$$

The integrals contain products of known constants coefficients and basis functions ϕ_ℓ and can thus be integrated exactly over T. For example,

$$\int_T \alpha_j\beta_k \mathrm{d}x = \sum_{m=1}^{10}\sum_{n=1}^{10} a_m^{(j)}b_n^{(k)}\int_T \phi_m\phi_n \mathrm{d}x = |T|a^{(j)^T}Mb^{(k)}$$

with the 10×10 mass matrix

$$M := 1/2520 \begin{pmatrix} 420 & 210 & 210 & 84 & 42 & 84 & 14 & 0 & -14 & 14 \\ 210 & 420 & 210 & 84 & 84 & 42 & -14 & 14 & 0 & 14 \\ 210 & 210 & 420 & 42 & 84 & 84 & 0 & -14 & 14 & 14 \\ 84 & 84 & 42 & 28 & 14 & 14 & 0 & 2 & -2 & 4 \\ 42 & 84 & 84 & 14 & 28 & 14 & -2 & 0 & 2 & 4 \\ 84 & 42 & 84 & 14 & 14 & 28 & 2 & -2 & 0 & 4 \\ 14 & -14 & 0 & 0 & -2 & 2 & 3 & -1 & -1 & 0 \\ 0 & 14 & -14 & 2 & 0 & -2 & -1 & 3 & -1 & 0 \\ -14 & 0 & 14 & -2 & 2 & 0 & -1 & -1 & 3 & 0 \\ 14 & 14 & 14 & 4 & 4 & 4 & 0 & 0 & 0 & 1 \end{pmatrix}.$$

According to (2.9) and the subsequent calculations, the second part of the local stiffness matrix reads

$$A^{(2)} = \frac{|T|}{12} \begin{pmatrix} 2 & 1 & 1 & 0 & 0 & 0 \\ 1 & 2 & 1 & 0 & 0 & 0 \\ 1 & 1 & 2 & 0 & 0 & 0 \\ 0 & 0 & 0 & 2 & 1 & 1 \\ 0 & 0 & 0 & 1 & 2 & 1 \\ 0 & 0 & 0 & 1 & 1 & 2 \end{pmatrix} \begin{pmatrix} 1 & 0 & 0 & 0 & 0 & 0 \\ 0 & 0 & 1 & 0 & 0 & 0 \\ 0 & 0 & 0 & 0 & 1 & 0 \\ 0 & 1 & 0 & 0 & 0 & 0 \\ 0 & 0 & 0 & 1 & 0 & 0 \\ 0 & 0 & 0 & 0 & 0 & 1 \end{pmatrix} D.$$

By definition of the ansatz functions, $\operatorname{div}\sigma_j$ equals some P_1 function with coefficients $d_\ell^{(j)}$, namely, for $j = 1,\dots,24$,

$$\operatorname{div}\sigma_j = \begin{pmatrix} d_1^{(j)}\phi_1 + d_3^{(j)}\phi_2 + d_5^{(j)}\phi_3 \\ d_2^{(j)}\phi_1 + d_4^{(j)}\phi_2 + d_6^{(j)}\phi_3 \end{pmatrix}.$$

For the coefficient matrix $D = (d^{(1)},\dots,d^{(24)}) \in \mathbb{R}^{6\times24}$ with $d^{(j)} = (d_1^{(j)},\dots,d_6^{(j)})^T$, there holds

$$D = \begin{pmatrix} L_1 & L_2 & L_3 & L_2 & 0 & L_3 & L_2 & 0 & -L_3 & 0 \\ L_1 & L_2 & L_3 & L_1 & L_3 & 0 & -L_1 & L_3 & 0 & 0 \\ L_1 & L_2 & L_3 & 0 & L_2 & L_1 & 0 & -L_2 & L_1 & 0 \end{pmatrix} X$$

with

$$X = (x^{(1)},\dots,x^{(24)}) \in \mathbb{R}^{30\times24},$$
$$x^{(j)} = (a_1^{(j)}, b_1^{(j)}, c_1^{(j)}, a_2^{(j)}, \dots, c_{10}^{(j)})^T \in \mathbb{R}^{30},$$
$$L_k := \begin{pmatrix} D_x\lambda_k & 0 & D_y\lambda_k \\ 0 & D_y\lambda_k & D_x\lambda_k \end{pmatrix}.$$

2.4. Local load vector and Neumann boundary conditions

Let $\mathscr{E}_D(T)$ denote the set of Dirichlet edges of the triangle T. Then the local load vector $b_T = (b_D, b_f)^T$ reads

$$\begin{aligned} b_{D,j} &:= \sum_{E\in\mathscr{E}_D(T)} \int_E u_D \cdot (\sigma_j v_E)\mathrm{d}s \quad \text{for } j = 1,\dots,24, \\ b_{f,k} &:= -\int_T f \cdot v_k \mathrm{d}x \quad \text{for } k = 1,\dots,6. \end{aligned} \tag{2.11}$$

Note that, in general, a one point Gauss quadrature of b_T does *not* lead to optimal convergence rates of the scheme and we suggest at least three Gauss point quadrature (in case of smooth data and otherwise even more accurate integration).

In the mixed formulation of (1.1), Neumann boundary conditions are essential conditions to be imposed strongly using Lagrange multipliers Ψ. With some boolean matrix B, with respect to the degrees of freedom which belong to the Neumann boundary, and some vector b_N the global linear system of equations reads

$$\begin{pmatrix} A & B^T \\ B & 0 \end{pmatrix}\begin{pmatrix} x \\ \Psi \end{pmatrix} = \begin{pmatrix} b \\ b_N \end{pmatrix}.$$

To satisfy $\sigma_h \in \Sigma_g$ it suffices to fix the degrees of freedom representing the integral mean of $\sigma_h v$ on each edge. Numerical experiments suggest that this leads to a suboptimal convergence order of $h^{1/2}$ as reported briefly in Fig. 3.4. To achieve an optimal convergence order of h^3, it is necessary to approximate g more accurately: fix the degrees of freedom corresponding to the moment of order one and the point evaluations $\sigma(P_i)$ of Section 3.2.

On each edge E on the Neumann boundary $\overline{\Gamma}_N$, one computes $b_N|_E = (d_1, d_2, d_3, d_4)^{\mathrm{T}}$ via

$$(d_1, d_2)^{\mathrm{T}} = |E|^{-1} \int_E g(x)\,\mathrm{d}s_x,$$

$$(d_3, d_4)^{\mathrm{T}} = |E|^{-2} \int_E ((x - \mathrm{mid}(E)) \cdot \tau_E) g(x)\,\mathrm{d}s_x.$$

For each node N on the Neumann boundary $\overline{\Gamma}_N$, we have to consider the three cases (a) – (c) of Fig. 2.2. If the Neumann node is either connected to the Dirichlet boundary (a) or the edges connected to it build a straight line (b) we have two equations $\sigma(N)v = g(N, v)$ for the three unknowns of $\sigma(N)$, which we include directly in our global system. In the third case, i.e., a corner node in the interior of the Neumann boundary (c), we have four equations $\sigma(N)v_{E_1} = g_{E_1}(N)$ and $\sigma(N)v_{E_2} = g_{E_2}(N)$, where $v_{E_{1,2}}$ denote the outer unit normal vectors of the two incident edges. In general, this over-determined system does not have a solution so we include the least square constraints in our global system of equations. For consistent data and a smooth stress, however, this computes the unique $\sigma(N)$.

A proper scaling of B with the lengthes of the Neumann edges preserves the condition number of the system.

2.5. Assembling the global linear system of equations

Given the regular triangulation $\mathcal{T}$ of Ω in the sense of Ciarlet [4,5,7,11] into triangles with the set of vertices $\mathcal{N}$ and the set of edges $\mathcal{E}$, the global degrees of freedom consist of

- (i) three dofs on each vertex for the nodal stress,
- (ii) four dofs on each edge for the edge stress moments of order 0 and 1,
- (iii) three dofs on each element for the integral mean of the stress,
- (iv) six dofs on each element for the (discontinuous) displacement.

The total number of degrees of freedom is $3|\mathcal{N}| + 4|\mathcal{E}| + 9|\mathcal{T}|$ with the cardinality or counting measure $|\cdot|$.

The global basis functions are defined by a unique global choice of the orientation of edges as vectors connecting the two end-points (P_1, P_2) in a fixed order. Since the computation of the local basis functions assumed outward pointing normals, one needs to subtract the entries corresponding to the edge stress moments of order 0 instead of adding them (the edge stress moments of order 1 do this automatically because of the oriented integration).

The resulting discretised weak form scales in the local stiffness matrix (2.7) in block $A^{(1)}$ like h^2 and in block $A^{(2)}$ like h (because of the divergence operator in the integrand). A multiplication of $A^{(2)}$ and the corresponding part of the right-hand side b_f with h_T, combined with a multiplication of the resulting coefficients of u_h with h_T to reverse this modification, takes care of this. The same procedure must also be applied to the data of edges on Γ_N to achieve the almost h independent condition numbers illustrated in Fig. 3.6.

Our implementation was performed in MATLAB in the spirit of [2,8,10].

3. Numerical experiments with Quasi-Uniform meshes

The first example illustrates the application of the Arnold–Winther MFEM to the classical Cook membrane problem while the second smooth academic example studies the experimental convergence rates for different treatments of the Neumann data.

3.1. Cook membrane problem

A tapered panel is clamped on one end and subjected to a surface load in vertical direction on the opposite end with $f = 0$ and $g(x, y) = (0, 1)$ if $(x, y) \in \Gamma_N$ with $x = 48$ and $g = 0$ on the remaining part of Γ_N, $E = 2900$, and $v = 0.3$. The linear elastic simulation is often called Cook's membrane problem, constitutes a standard test for bending dominated response. Fig. 3.2 displays the deformed mesh and a grey scale for the modulus of the deviatoric part of the stress approximation based on a mesh $\mathcal{T}_1 := \mathrm{red}(\mathcal{T}_0)$ and $\mathcal{T}_0$ from Fig. 3.1. A red refinement divides each triangle into four congruent sub-triangles by connecting the three edges' midpoints through straight lines.

3.2. Optimal convergence rates

This example with known smooth solution illustrates empirical convergence rates and robust approximation for $v \to 1/2$. Given the unit square $\Omega = (0, 1)^2$ with $\Gamma_D = \{0\} \times [0, 1]$ and $\Gamma_N = \partial\Omega \setminus \Gamma_D$ of Fig. 3.3, let the elastic modulus be $E = 10^5$ and the Poisson ratio be $v = 0.3$,
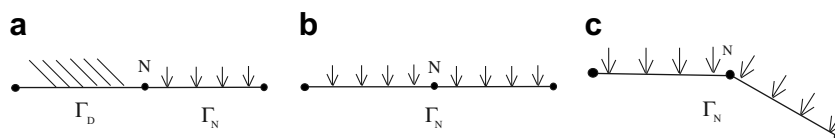

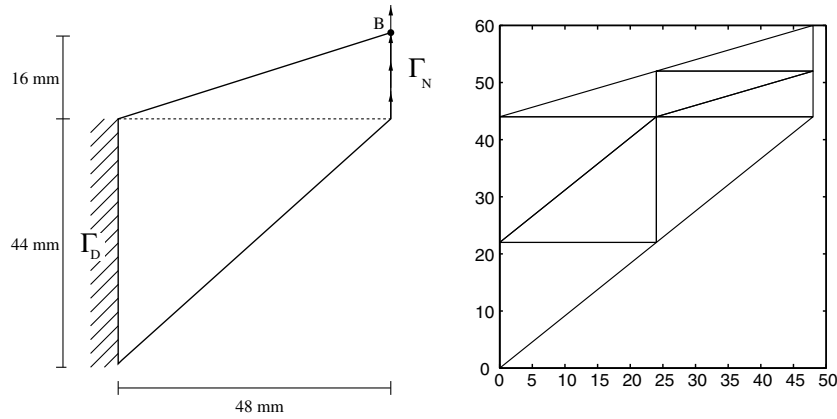Fig. 2.2. Different neighbourhoods of a Neumann node N.

Fig. 3.1. Cook's membrane problem. Geometry (left) and initial mesh (right).
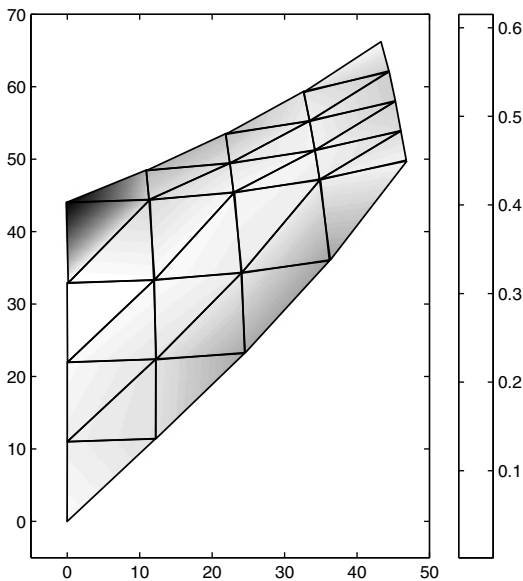

Fig. 3.2. Deformed mesh with a magnification factor of 50 and $|\text{dev}(\sigma_h)|$ in a gray scale for the deviatoric part $\text{dev}(\sigma_h)$ of σ_h in Section 3.1.

and choose the data f, g, and u_D in such a way that the exact solution reads $u = \sin(2(x+1))\cos^2(y+1)$, $\cos(\pi(x+1))$ $\sin^2(y+1))$ and belongs to $H^2(\Omega)^2$.

The sequence of meshes is generated uniformly by $\mathcal{T}_0$ from Fig. 3.3 through successive red refinements. Fig. 3.4 repeats various convergence rates for different discretisations of the Neumann conditions as discussed in Section 2.4. Different treatments exhibit various experimental convergence rates of h^3, $h^{3/2}$, and $h^{1/2}$ for the stress error (left), while rates of h^2, h^2, and h for the displacement error (right). The conclusion is that it pays off to treat the boundary conditions with full care of Section 2.4: One needs to fix the stress approximations in all nodal values on $\overline{\Gamma}_N$ and the moment conditions for each edge on $\overline{\Gamma}_N$.

To test the locking-free approximation, various Poisson ratios are tested and reported in Fig. 3.5. For different choices of $v = 0.3, 0.49$, and 0.499, the relative stress error $\|f\|_{L^2(\Omega)}^{-1}\|\sigma - \sigma_h\|_{L^2(\Omega)}$ coincides for all error graphs with an experimental convergence rate of h^3. The displacement error $\|u - u_h\|_{L^2(\Omega)}$ (right) coincides asymptotically for different choices of v with an experimental convergence rate of h^2.

3.3. Notes on the condition number

A formulation of the problem with Neumann boundary condition seems to lead to an almost v-independent condi-
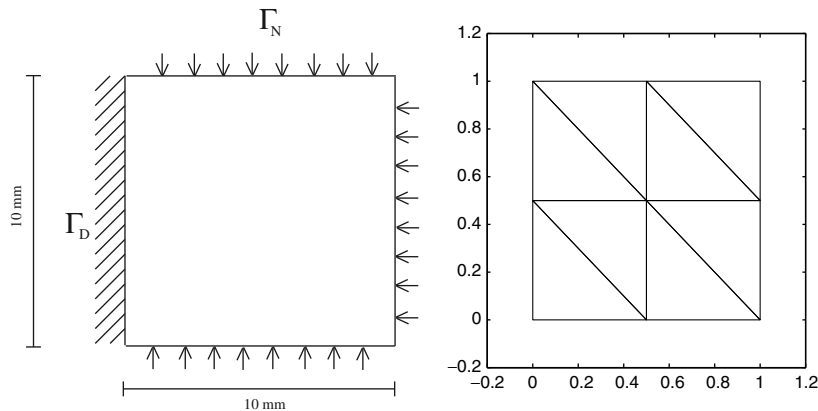

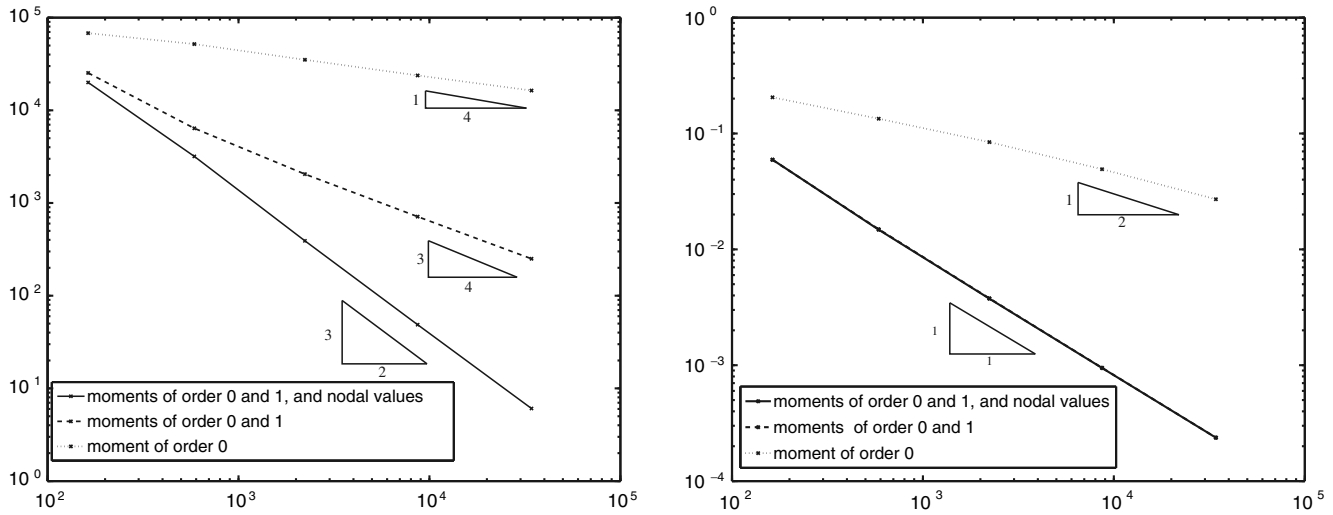Fig. 3.3. Smooth benchmark problem of Section 3.2. Geometry (left) and initial mesh (right).

Fig. 3.4. Convergence history in Section 3.2 for the stress error $\|\sigma - \sigma_h\|_{L^2(\Omega)}$ (left) and the displacement error $\|u - u_h\|_{L^2(\Omega)}$ (right) plotted as functions of the numbers of degrees of freedom both in logarithmic scalings.
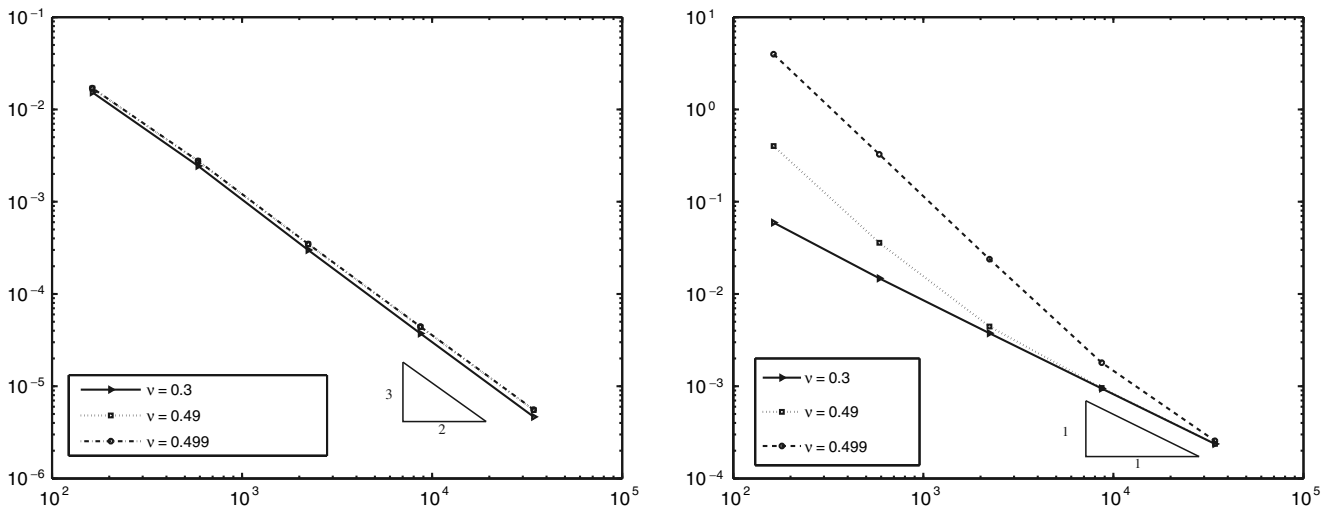

Fig. 3.5. Illustration of the robust convergence behavior in the Poisson ratio v for the example of Section 3.2 for the stress error (left) and the displacement error (right).

tion number of A as seen in Fig. 3.6. For the different problem with $\partial\Omega = \Gamma_D$, and u_D and f from the same exact solution u of Section 3.2, which we do not display for brevity, we observed that $\text{cond}(A) \to \infty$ as $v \to 1/2$.

4. Numerical experiments with graded meshes

Corner singularities enforce lower experimental convergence rates for uniform meshes. The first subsection studies some benchmark on the L-shaped domain for a uniform mesh. It is commonly believed that a class of graded meshes [4] improves the convergence rates. However, Section 4.2 illustrates that the meshes are too degenerated for large grading parameters. A graded mesh algorithm is introduced which leads to optimal convergence.

4.1. Benchmark on L-shaped domain

The L-shaped domain Ω of Fig. 4.1 with $\Gamma_D = \partial\Omega$ gives rise to a singularity at the re-entrant corner. Using polar coordinates (r, θ), $-\pi < \theta \leqslant \pi$ the exact solution u with radial component u_r reads

$$u_r(r, \theta) = \frac{r^\alpha}{2\mu}(-(\alpha + 1)\cos((\alpha + 1)\theta)$$
$$+ (C_2 - (\alpha + 1))C_1 \cos((\alpha - 1)\theta)),$$
$$u_\theta(r, \theta) = \frac{r^\alpha}{2\mu}((\alpha + 1)\sin((\alpha + 1)\theta)$$
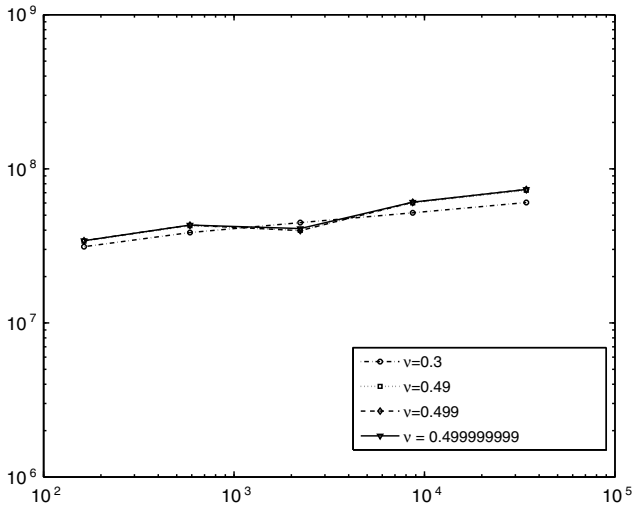$$+ (C_2 + \alpha - 1)C_1 \sin((\alpha - 1)\theta)).$$

Fig. 3.6. Condition number of the global stiffness matrix A vs. degrees of freedom for different choices of v and all other data as in Section 3.2. For $v \to 1/2$ the graphs almost coincide between 10^7 and 10^8.

The parameters are $C_1 = -\cos((\alpha+1)\omega)/\cos((\alpha-1)\omega)$, $C_2 = 2(\lambda+2\mu)/(\lambda+\mu)$, where $\alpha = 0.54448\ldots$ is the positive solution of $\alpha \sin 2\omega + \sin 2\omega\alpha = 0$ for $\omega = 3\pi/4$; the Young modulus is $E = 10^5$, the Poisson ratio is $v = 0.3$, and the volume force is $f \equiv 0$. The sequence of red-refined uniform meshes is based on $\mathcal{T}_0$ of Fig. 4.1. The resulting stress and displacement errors are shown in Fig. 4.2 for various values of the Poisson ratio $v = 0.3, 0.49,$ and 0.499. In contrast to Section 3.2, the convergence rates are far from optimal which is expected in the presence of the corner-singularity.

4.2. Graded meshes

The convergence rates of uniform triangulations are limited because of corner-singularities (see Fig. 4.2). To obtain the optimal convergence rates of Section 4.1, a graded mesh as in Fig. 4.3 is necessary. Note that in β-graded meshes, which are usually employed, the minimum angle
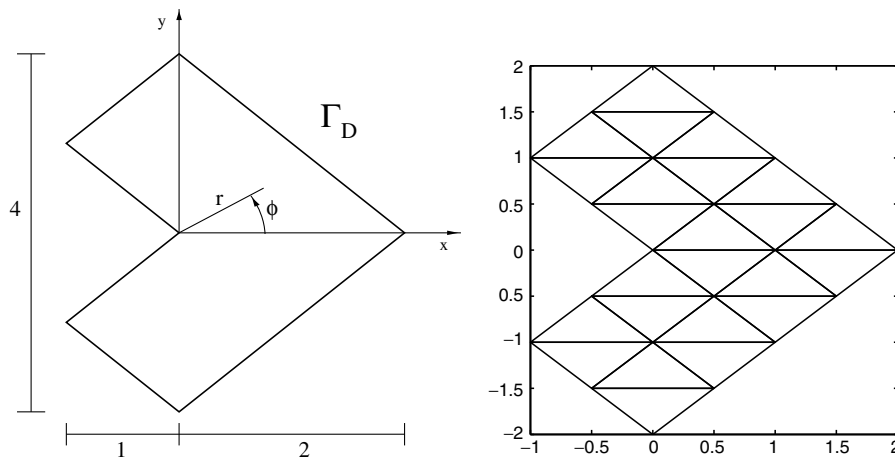

Fig. 4.1. Model problem exhibiting a corner singularity. System and initial mesh.
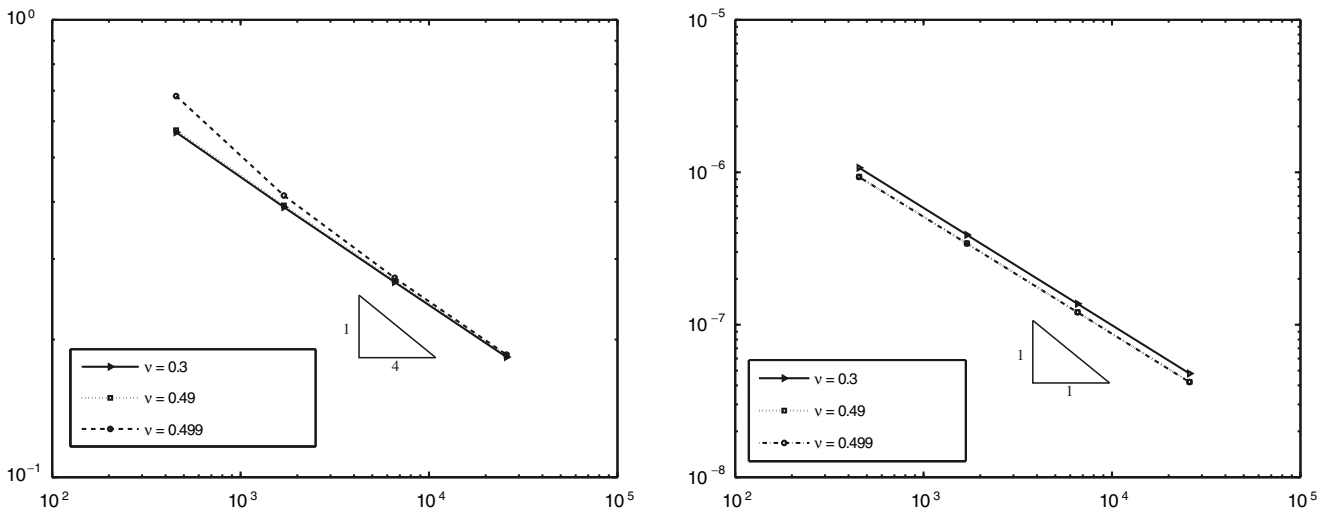

Fig. 4.2. Convergence history in Section 4.1 for the stress error $\|\sigma - \sigma_h\|_{L^2(\Omega)}$ (left) and the displacement error $\|u - u_h\|_{L^2(\Omega)}$ (right) plotted as functions of the numbers of degrees of freedom in both axes with logarithmic scalings for uniform refinements of a L-shaped domain.
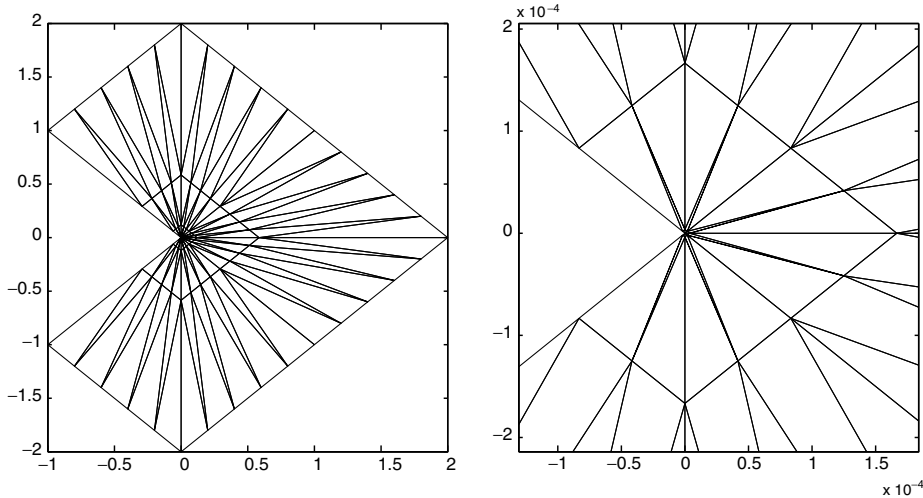
Fig. 4.3. Six graded mesh which results in optimal convergence rates in Section 4.2 with a zoom near the re-entering corner on the right.

depends strongly on β. Because we are dealing with a higher-order method, $\beta = 6$ is large if one wants to obtain optimal convergence rates, and therefore leads to huge condition numbers (not displayed). This limited the applicability of the MFEM dramatically. (see Fig. 4.4)

To circumvent this difficulty we employ the newest vertex bisection to obtain a mesh which exhibits optimal convergence rates while the minimum angle depends only on the initial triangulation.

Algorithm GRADMESH. Input: Grading parameter $0 < \mu < 1$, global mesh-size H, initial triangulation $\mathcal{T}$

Until $\mathcal{M} = \emptyset$ do
(i)
$\mathcal{M} := \{E \in \mathcal{E}(\mathcal{T}) | \exists T \in \mathcal{T} \text{ with } E \subseteq \partial T \text{ and diam}(T) > H|\text{mid}(T)|^{\mu}\}$
(ii) $\mathcal{T} = \text{newestVertexBisection}(\mathcal{T}, \mathcal{M})$ od
Output: Triangulation $\mathcal{T}$.

The algorithm GRADMESH generates a mesh which is refined locally towards the origin, but can be modified for a more general situation. For details on newest vertex

bisection we refer to [4]. In the present examples, the strategy leads to right isosceles triangles and is similar to the classical red-green-blue refinement. From the marking strategy in step (i) of GRADMESH it follows that the typical grading property $\text{diam}(T) \leqslant H|\text{mid}(T)|^{\mu}$ holds for all $T \in \mathcal{T}$ with center of mass $\text{mid}(T)$. Note that the grading parameter μ is chosen independently of the parameters in a β-grading.

4.3. Benchmark on L-shaped domain on graded meshes

The algorithm GRADMESH run with a grading parameter $\mu = 0.9$ on the L-shaped domain results in an optimal experimental convergence rate. In fact, all error graphs almost coincide with respective experimental convergence rates of h^4 and h^2 in Fig. 4.5. This is a surprisingly fast and robust empirical convergence.

It is conjectured that the right-hand side $f = 0$ in this example might result in a higher-order convergence h^4 in the stress error of Fig. 4.5.
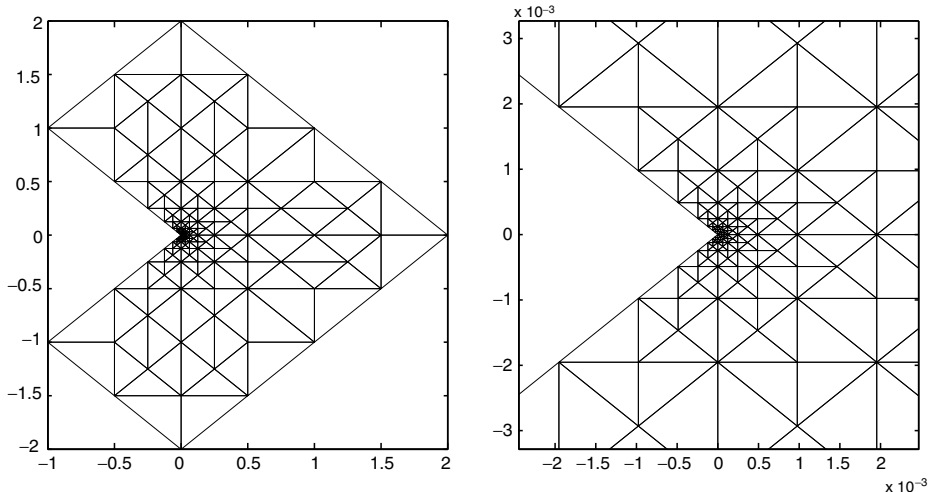

Fig. 4.4. Mesh produced by algorithm GRADMESH (left) with a zoom near the re-entering corner on the right.
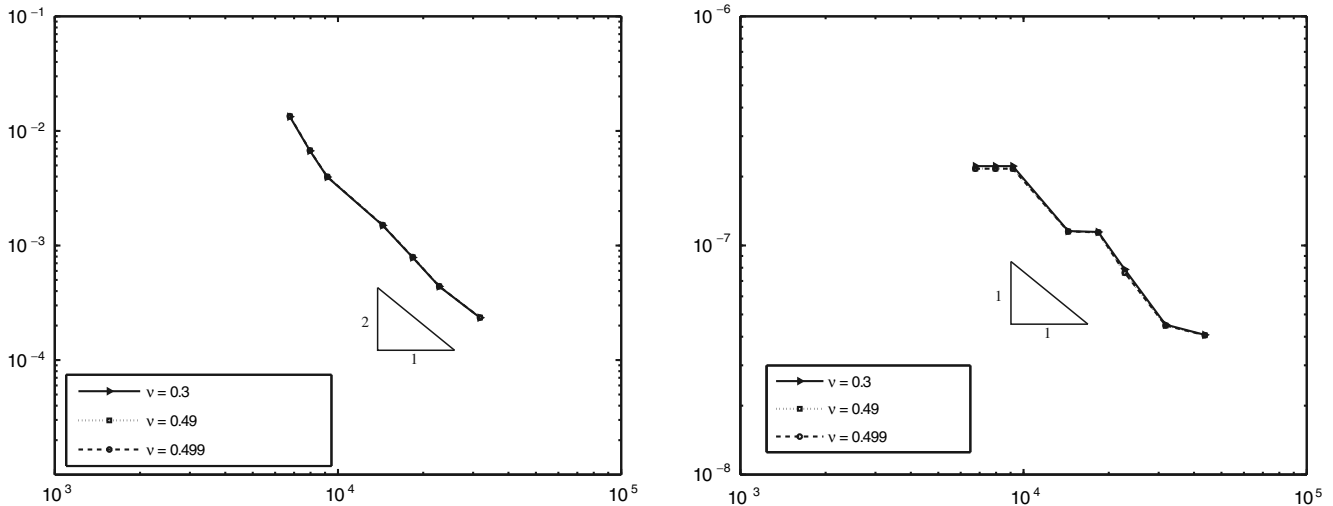
Fig. 4.5. Convergence history for the stress error $\|\sigma - \sigma_h\|_{L^2(\Omega)}$ (left) and the displacement error $\|u - u_h\|_{L^2(\Omega)}$ (right) of Section 4.3 plotted as functions of the numbers of degrees of freedom both in logarithmic scalings for different choices of $v = 0.3, 0.49, 0.499$.

5. Conclusions

(a) This paper supports the theoretical predictions and expectations for uniform and graded meshes. The convergence rates confirm the proven robustness as $\lambda \to \infty$ (see Figs 3.5 and 4.5); in conclusion, the symmetric MFEM overcomes locking.

(b) As illustrated in Fig. 3.4, various treatments of Neumann boundary conditions of Section 2.4 lead to suboptimal convergence phenomena.

(c) Our numerical experiments suggest the conjecture that for some right-hand-sides (e.g. $f \equiv$ const), the empirical stress convergence rates are super-optimal (cf. Fig. 4.5).

(d) The suggested discrete system appears to be reasonably conditioned, the condition number seems λ and h-independent (cf. Fig. 3.6) for small numbers of degrees of freedom as a result of the scaling described in Section 2.5.

(e) Our numerical experience demonstrates that the use of the Arnold–Winther MFEM can indeed be recommended to practitioners for various applications in solid mechanics.

Acknowledgement

References

[1] D.N. Arnold, F. Brezzi, J. Douglas, PEERS: a new finite element for plane elasticity, Jpn. J. Appl. Math. 1 (1984) 347–367.

[2] J. Alberty, C. Carstensen, S.A. Funken, R. Klose, Matlab implementation of the finite element method in elasticity, Computing 69 (2002) 239–263.

[3] D. Arnold, R. Winther, Mixed finite elements for elasticity, Numer. Math. 92 (2002) 401–419.

[4] S. Brenner, C. Carstensen, Finite element methods, Encyclopedia of Computational Mechanics, John Wiley & Sons, 2004, Chapter 4 therein.

[5] S.C. Brenner, L.R. Scott, The mathematical theory of finite element methods, Texts in Applied Mathematics, vol. 15, Springer, New York, 1994.

[6] F. Brezzi, M. Fortin, Mixed and Hybrid Finite Element Methods, Springer-Verlag, 1991.

[7] D. Braess, Finite Elements – Theory, Fast Solvers and Applications in Solid Mechanics, Cambridge University Press, 2001.

[8] C. Carstensen, C. Bahriawati, Three Matlab implementations of the lowest-order Raviart–Thomas MFEM with a posteriori error control, Comput. Meth. Appl. Math. 5 (4) (2005) 333–361.

[9] C. Carstensen, G. Dolzmann, A posteriori error estimates for the mixed FEM in elasticity, Numer. Math. 81 (1998) 187–209.

[10] C. Carstensen, G. Dolzmann, S.A. Funken, D.S. Helm, Locking-free mixed finite element methods in linear elasticity, Comput. Meth. Appl. Mech. Engrg. 190 (2000) 1701–1781.

[11] P.G. Ciarlet, The Finite Element Method for Elliptic Problems, North-Holland, Amsterdam, 1978.

[12] R. Stenberg, A family of mixed finite elements for the elasticity problem, Numer. Math. 53 (1988) 513–538.